CrystEngComm

Accepted Manuscript

ROYAL SOCIETY OF CHEMISTRY

www.rsc.org/crystengcomm

Journal Name

RSCPublishing

ARTICLE

Density functional theory study of the magnetic shielding mechanism for ^{11}B in pentaborate minerals: ulexite and probertite

Cite this: DOI: 10.1039/xoxxoooooox

Received ooth January 2012,
Accepted ooth January 2012

DOI: 10.1039/xoxxoooooox

www.rsc.org/

B. Zhou,[ab*] V. K. Michaelis,[c†] YefengYao,[d] Barbara L. Sherriff,[e] Scott Kroeker,[c] and Yuanming Pan[f*]

Nuclear magnetic resonance (NMR) parameters of ^{11}B in borates and borosilicates, unlike those of many other nuclei such as ^{29}Si and ^{27}Al, vary only in limited ranges for a given polyhedral geometry, but mechanisms for such insensitivity to local structural environments remain poorly understood. In this contribution, ulexite and probertite with the ($[B_5O_6(OH)_6]^{3-}$) pentaborate polyanion as the fundamental building block have been investigated in detail by *ab initio* theoretical calculations of the density of states (DOS) as implemented in WIEN2k, including optimization of the structures and determination of contributions to the magnetic shielding at the five distinct B sites each. Calculated ^{11}B NMR parameters of these two pentaborates are compared with high-precision experimental data obtained at high (14 T) and ultrahigh (21 T) fields. Optimized structures using the linearized augmented plane-wave method with additional radial basis functions in the form of local orbitals (i.e., LAPW+LO) not only yield more accurate electric field gradients (EFG) at the distinct three- and four-fold-coordinated B sites (i.e., [BO_3] or $^{[3]}$B and [BO_4] or $^{[4]}$B] but also improve the calculated ^{11}B magnetic shielding. In particular, the magnetic shielding variation trends among the B sites in ulexite and probertite are determined mainly by the valence states and especially by the local *p* orbitals of B and its nearest-neighbor O atoms. Calculations with the water molecules removed or K^+ substituting for Na^+ in the structures show that the next-nearest-neighbor cations and water molecules have negligible effects. Theoretical calculations also reveal that the systematic differences in shielding between $^{[3]}$B and $^{[4]}$B are caused by multiple factors such as the occupancies and imbalance of the *sp* hybrid orbitals between B and its nearest-neighbor O atoms.

1. Introduction

Because of the high sensitivity of nuclear magnetic resonance (NMR) parameters such as chemical shifts (and quadrupolar interaction (QI) parameters as well, if the nuclear spin number I ≥1) to the details of the geometric and electronic structures, solid-state NMR is a very powerful technique not only for structural determination but also for probing subtle structural differences and disorder in minerals and other materials.[1,2]Also, *ab initio* Density Functional Theory (DFT) calculations have become increasingly helpful in quantitative understanding of chemical shifts and other NMR parameters and enabling the full power of NMR spectroscopy to be exploited.[3] This is especially true for solids having multiple sites with the same multiplicity, where empirical rules are difficult to develop.[4,5] As such, the popularity of DFT calculations has in recent years formed a link between NMR and crystallography, leading to the formalization of "NMR crystallography".[3-6]

^{11}B NMR parameters in borates and borosilicates, however, generally show limited variations and, hence, have been thought to be incapable of providing structural information beyond the first shell.[7,8] Due to recent advances in NMR techniques as well as progresses in quantum mechanical theoretical calculations, interest in ^{11}B NMR for local structural characteristics in borates has been rekindled.[9-13] For example, high resolution ^{11}B Magic Angle Spinning (MAS) NMR spectra of borate minerals such as ulexite and probertite have been obtained at high and ultra-high magnetic fields (14 and 21 T)[11-13]. Although these borates with the polyanion $[B_5O_6(OH)_6]^{3-}$ as the fundamental building block (FBB) (Fig. 1) have three crystallographically distinct four-fold-coordinated B ($^{[4]}$B) sites,[14,15] their ^{11}B NMR spectra are characterized by a single broad resonance centered at ~1 ppm in both fields of 14 and 21 T, with the latter having a hint of asymmetry in the $^{[4]}$B peak attributable to the greater chemical shift dispersion at the higher field.[11-13] On the other hand, the 21 T spectra clearly resolve the two three-fold-coordinated B ($^{[3]}$B) sites compared with its 14 T

counterparts due to the reduction of second order QI and therefore the full width at the higher field.[11-13] Fast MAS and high-power proton decoupling eliminate homo- and hetero-

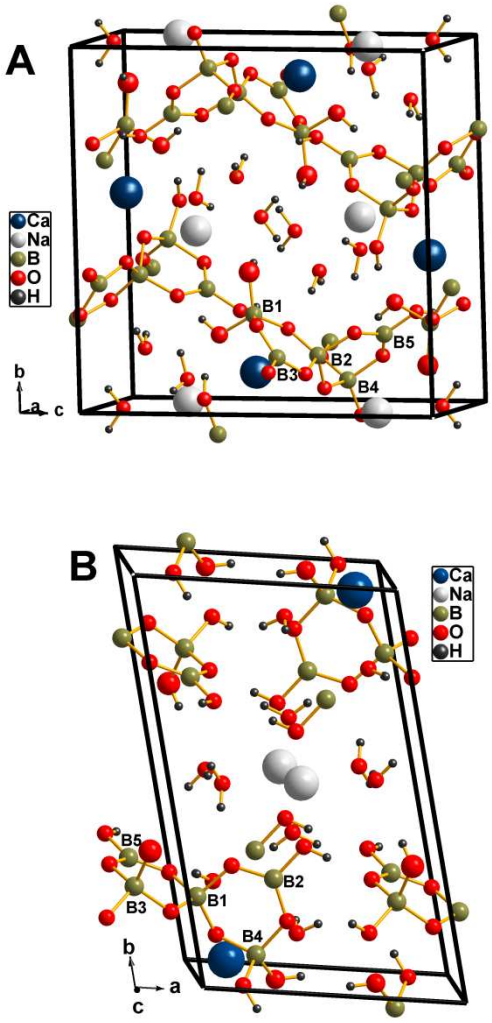

Fig. 1 Crystal structures of (A) probertite and (B) ulexite, with the five distinct B sites in both FBB labeled.

nuclear dipolar effects, respectively, bringing us to the limit of the MAS NMR spectral resolution at the B sites and so giving the very accurate experimental NMR parameters.

Theoretical calculations of the electric field gradients (EFG) at different [3]B and [4]B sites have determined the contributions to the QI parameters of ^{11}B in ulexite.[13]However, there have been no previous theoretical studies to quantitatively determine the magnetic shielding mechanism of ^{11}B in borates or borosilicates. Interestingly, recent studies have successfully evaluated the origins for the chemical shielding contributions at ^{19}F, ^{17}O, $^{35/37}$Cl and $^{79/81}$Br in fluorides, oxides, chlorides and bromides, respectively.[16-20] In this contribution, we expand on our previous theoretical study on EFG at different [3]B and [4]B sites in ulexite and perform detailed DFT magnetic shielding calculations on two pentaborate minerals of probertite and ulexite,[14,15]in order to determine the mechanisms responsible for the insensitivity of ^{11}B chemical shifts to local structural environments. These two pentaborates are selected for the following three reasons: 1) multiple crystallographically distinct [3]B and [4]B sites, 2) different FBBs (i.e., neso-pentaborate versus ino-pentaborate), and 3) available high-resolution ^{11}B chemical shifts from MAS NMR experiments at ultra-high fields. Magnetic shielding calculations, unlike EFG calculations involving the ground states only, also include the excited states (orbitals) and are, therefore, more complicated and informative.

2. Theoretical Calculation Background

Induced magnetic field at a nucleus due to the external field **B** is expressed as follows:[16-19]

$$\mathbf{B}_{ind}(\mathbf{R}) = -\overleftrightarrow{\sigma}(\mathbf{R})\mathbf{B} = \frac{1}{c}\int d^3r \mathbf{j}_{ind}(\mathbf{r}) \times \frac{\mathbf{R}-\mathbf{r}}{|\mathbf{R}-\mathbf{r}|^3} \quad (1)$$

with $\overleftrightarrow{\sigma}$ being the absolute chemical shift tensor and the induced current $\mathbf{j}_{ind}(\mathbf{r})$ in the first perturbation being in the form of:

$$\mathbf{j}_{ind}(\mathbf{r}') = \sum_o \left[\left\langle \Psi_o^{(1)} \middle| \mathbf{J}^{(0)}(\mathbf{r}') \middle| \Psi_o^{(0)} \right\rangle + \left\langle \Psi_o^{(0)} \middle| \mathbf{J}^{(0)}(\mathbf{r}') \middle| \Psi_o^{(1)} \right\rangle + \left\langle \Psi_o^{(0)} \middle| \mathbf{J}^{(1)}(\mathbf{r}') \middle| \Psi_o^{(0)} \right\rangle \right] \quad (2)$$

and

$$|\Psi_o^{(1)}\rangle = \sum_e |\Psi_e^{(0)}\rangle \frac{\langle \Psi_e^{(0)} | H^{(1)} | \Psi_o^{(0)} \rangle}{E_o - E_e} \quad (3)$$

with

$$H^{(1)} = \frac{1}{2c}\mathbf{r}\times\mathbf{p}\cdot\mathbf{E} \quad (4)$$

These formulas are the foundation for the analysis of magnetic shielding mechanisms. In order to gain insight into the underlying NMR shielding mechanisms and distinguish the contributions arising from the local structural effects from the long-range effects in crystals, attempts have been made to decompose the NMR shielding into different local orbitals and energy windows.[4,16-19]

Generally speaking, there are two kinds of wavefunction-based models for the theoretical calculations of magnetic shielding (i.e., chemical shift): the molecular orbital (MO) approach and models with considerations of the periodic boundary conditions in crystals. The MO approach used here is the cluster hybrid-DFT method. Although the simple MO method has clearly proven its usefulness in gaining insights into relationships between NMR parameters and local structural features, it is difficult to account for the long range intermolecular or electrostatic interactions in solids due to the limitation of cluster approximation.[4] The periodic calculation approach, on the other hand, by taking the shielding contributions from the nearest neighbors as well as the long-range electrostatic interactions into account during NMR calculations, can evaluate the geometric and electronic structures of crystalline materials by comparison with available NMR experimental data.[20]

In this context, gauge including projector augmented waves (GIPAW) adopts a relatively simple plane-wave basis set with approximated pseudo-potentials during NMR parameter calculations for periodic structures, and its actual implementation is gauge invariant and so the results do not

depend on the choice of the unit-cell origin.[17] Consequently, GIPAW is quickly becoming an essential tool for interpreting and understanding experimental NMR spectra by providing reliable assignments of the observed resonances to crystallographic sites or enabling a priori prediction of NMR data.[3,4,21,22,23]Although previous studies obtained agreements between localized and plane-wave basis sets,[24] Charpentier[5] noted that the use of plane-wave expansion smears localized features (in contrast to the use of localized basis sets),which could mask contributions to the shielding. The ultra-soft pseudo-potential describing the interactions between core and valence electrons may also lead to unphysical behavior and thus misleading conclusions from GIPAW modeling.[5]

As an alternative method for periodic systems, the calculations presented in this work have been mainly carried out using the WIEN2k code.[1,7-19]For this full-potential and all-electron method, the electronic potential in the unit cell is partitioned into non-overlapping atom-centered spheres and an interstitial area between the spheres (Muffin-Tin partition), no approximation to either the potential or charge density is made, and the exchange and correlation effects are treated by DFT using the generalized gradient approximation (GGA). A linear combination of the products of radial functions and spherical harmonics is then used inside the atomic spheres, and a plane-wave expansion is used in the interstitial area as the basis sets.[25-27] Finally, the Kohn-Sham equations[28] and hence the crystal wavefunctions are solved by the variational principle, and thus the electronic structure can be obtained. For NMR calculations using this method, the current operator obtained from the quantum mechanical probability induced by the external magnetic field, which results in the magnetic shielding, can be written as the sum of diamagnetic and paramagnetic terms.[3] There is no restriction or any approximation imposed on the induced current density and the integration of all electrons for this linearized augmented plane-wave (LAPW) method, however, additional radial basis functions in the form of so-called local orbitals (LO) of *s*, *p*, and *d* characters have been added to the basis set.[18] This method will be referred to as LAPW+LO hereafter.

For the cluster hybrid-DFT method without the considerations of crystal periodicity, the complete Gaussian atomic functions are used as the basis sets for the molecular wave functions or orbitals of the cluster chosen.[23,29] Using the Becke-style 3-Parameter DFT with Lee-Yang-Parr (B3LYP) functional energy levels for the correlation and exchange interactions,[29,30] EFG and magnetic shielding for the clusters can be calculated through the variational principle.[31-36]

3. Calculation Procedures

For the Full Potential (FP) LAPW calculations using the WIEN2k software package in this study, the atomic coordinates of ulexite and probertite from the X-ray diffraction (XRD) studies of Ghose *et al.*[14] and Menchetti *et al*.[15] were taken as the input data. The following atomic-sphere radii (*RMT*), given in atomic units (a.u.), were used so that the calculations ran with the highest efficiency without any core charge leakage occurring: H (0.65), B (1.3), O (1.6), Na (2.2) and Ca (2.3). The core electron states were separated from the valence states at -6.0 Ry. All calculations are based on the LAPW+LO method and DFT with PBE exchange correlation functional. Calculations were performed at a plane-wave cut-off defined by min(*RMT*)*max(K_n) of 3.5, where K_n is the *k* vector; such a cut-off value corresponds to approximately 10,000 plane waves for minerals. In all calculations, the irreducible Brillouin Zone was sampled on shifted tetrahedral meshes at 32 *k*-points, which is expected to achieve a good convergence for insulators. Angular momentum components up to *l*=12 were included for the wave functions inside the atomic spheres. The self-consistent field (SCF) calculations were run in a non-spin-polarized mode and the convergent condition for SCF was set at 2×10^{-5} eV. All of the above set-ups have been shown to be adequate for producing stable and convergent results. The optimization employed the experimental XRD fractional atomic coordinates as the starting values and kept the unit cell parameters unchanged. The retention of the unit cell parameters from room-temperature XRD experiments[14,15] (vs. default athermal relaxation to 0 K) is intended to facilitate direct comparison with data obtained room-temperature NMR spectra.[11-13] Using a definition of the incremental interval, the atomic coordinates were optimized by reducing the forces acting on the atoms to less than 1 mRy/a.u.. In addition, "computer experiments" involving the removal of one or more water molecules from the ulexite and probertite structures (i.e., dehydration) were done to investigate the effects of the H_2O molecules on the magnetic shielding at ^{11}B and ^{23}Na. Similarly, LAPW+LO calculations for the pentaborates with K^+ substituting for Na^+ have also been performed by WIEN2k. The GIPAW calculation procedure is the standard one using the CASTEP package: PBE for exchange-correlation interactions, 32 *k*-point mesh, 2×10^{-5} eV of SCF convergence condition.

All of these calculations were first performed on a multi-node cluster of computers (16 nodes with a total of 256 cores) at the Shanghai Super Computer Center (SSC) with the Quad-Core AMD Opteron^{tm} Processor 2350 at 2 GHz and 1024 GB RAM. Subsequently, some WIEN2k calculations also have been performed on the Grex SGI Altix XE 1300 cluster containing 316 nodes, each with two 6-core Intel Xeon X5650 2.66 GHz processors with 48 to 96 GB of memory, at Compute Canada's Westgrid high performance computing facility.

In addition, the cluster hybrid-DFT modeling has been done to investigate the effects of local orbitals on NMR parameters. A charge-neutral FBB cluster with 25 atoms for ulexite[14] was constructed for the cluster hybrid-DFT calculations using the software Gaussian98W at a theoretical level of B3LYP using the gauge including atomic orbital (GIAO) method and basis set of 6-311G+d** (hybrid-DFT).[23,29] These SCF cluster hybrid-DFT calculations were performed on a personal computer with a 2.26 GHz processor and 3 GB RAM. The cluster hybrid-DFT calculations have also been attempted for probertite but were not successful, because its charge-neutral FBB cluster is difficult to optimize.

4. Results and Discussion

4.1. DFT structural optimization of probertite

Similar to our previous study of ulexite,[13] WIEN2k optimizations of probertite resulted in significant decreases of the forces on all atoms in the unit cell, reducing the average values of 542 mRy/a.u. (with the maximum of 1577 mRy/a.u.) for the original XRD structure to only 1 mRy/a.u for the optimized counterpart. However, the reductions in the forces on the H atoms are larger in comparison with the other atoms. Table 1 compares the optimized fractional atomic coordinates for probertite with the XRD data.[15]As with ulexite,[13] the optimized positions of the Ca, Na, O and B atoms in probertite differ from the XRD data[15] at the third decimal place or less than 1%. However, larger changes are observed for the H atoms (such as H9: 32%, H10: 9.2%, H7: 4.5%).The comparisons between the bond lengths of B-O, Na-O, Ca-O and O-H before

and after the optimization for probertite are listed in Tables S1 and S2, which show the largest B-O bond distance deviations for the [BO_3] and [BO_4] groups in probertite are less than 0.0165 and 0.0183 Å, respectively, while that for Ca-O6 at 0.0387 Å is the largest deviation in distance among the O-B, O-Ca and O-Na bonds (Table S1). Table S1 also shows that the average B-O bond distances for all B sites in the optimized probertite structure are systematically ~0.01 Å shorter than those from XRD.

Table 1 LAPW+LO - optimized fractional atomic coordinates for probertite

Atom	x/a	y/b	z/c
Ca	0.3534(0.3483)	0.5884(0.5878)	0.0948(0.0950)
Na	0.1176(0.1210)	0.4971(0.4956)	0.3241(0.3243)
OH1	0.7825(0.7867)	0.5060(0.5057)	0.4057(0.4092)
OH2	0.1714(0.1737)	0.6394(0.6419)	0.4390(0.4357)
O3	0.3307(0.3323)	0.2980(0.2970)	0.8498(-0.1491)
O4	0.3471(0.3497)	0.1237(0.1257)	0.9356(-0.0627)
O5	0.1394(0.1431)	0.2605(0.2618)	0.9841(-0.0147)
O6	0.5134(0.5135)	0.2852(0.2866)	0.0187(0.0180)
O7	0.2860(0.2887)	0.4000(0.3994)	0.0983(0.0986)
O8	0.6277(0.6299)	0.4533(0.4526)	0.1012(0.0999)
O9	0.5552(0.5612)	0.2979(0.2979)	0.2010(0.1991)
O10	0.9202(0.9254)	0.3803(0.3805)	0.0481(0.0490)
O11	0.9006(0.9003)	0.3732(0.3738)	0.2275(0.2267)
O*w*12	0.7912(0.7956)	0.2497(0.2486)	0.3453(0.3412)
O*w*13	0.9642(0.9633)	0.5408(0.5398)	0.1526(0.1521)
O*w*14	0.4284(0.4330)	0.5702(0.5700)	0.2777(0.2789)
B1	0.3376(0.3383)	0.2409(0.2414)	0.9482(-0.0514)
B2	0.4978(0.5012)	0.3576(0.3576)	0.1038(0.1030)
B3	0.1173(0.1207)	0.3492(0.3486)	0.0438(0.0448)
B4	0.8516(0.8535)	0.4400(0.4396)	0.1333(0.1327)
B5	0.7525(0.7554)	0.3095(0.3092)	0.2561(0.2542)
H1	0.351(0.346)	0.250(0.256)	0.794(-0.199)
H2	0.488(0.466)	0.101(0.105)	0.931(-0.067)
H3	0.935(0.902)	0.255(0.255)	0.385(0.372)
H4	0.866(0.882)	0.599(0.597)	0.161(0.161)
H5	0.447(0.461)	0.646(0.643)	0.299(0.292)
H6	0.560(0.536)	0.536(0.543)	0.311(0.304)
H7	0.804(0.798)	0.443(0.447)	0.452(0.450)
H8	0.744(0.755)	0.560(0.555)	0.454(0.455)
H9	0.048(0.070)	0.678(0.675)	0.453(0.448)
H10	0.283(0.259)	0.696(0.692)	0.450(0.446)

*Coordinates in parentheses are those from single-crystal XRD.[15]

Previous studies show that the quadrupolar coupling constant (C_Q) and asymmetry (η) parameters of the $^{[3]}$B and $^{[4]}$B sites calculated from the optimized structures are in better agreement with the NMR experimental values than those calculated directly from the XRD structures of ulexite and other borate minerals.[11-13]Similarly, the C_Q values of 2.55 MHz for $^{[3]}$B in probertite calculated from the optimized structure, in comparison with those (2.31 MHz) obtained from the original XRD structure, are in better agreement with the experimental result of 2.61 MHz,[11] supporting that the optimized structure is more accurate.

Better structural accuracy gained by optimization is also reflected in the more realistic hydrogen bonding geometries. The largest change of the hydrogen bond distances in probertite (Table S2) after the structural optimization using LAPW+LO is the O3-H3 bond with the variation of 0.2799 Å, and all of the donor(D)-H distances from the XRD structure become systematically longer after the optimization with the largest variation of 0.2518 Å (O10-H3) and the smallest variation of 0.0532 Å (O*w*12-H5). Because of the significantly stronger hydrogen bonding (Table S2), the water molecules in probertite exert greater influence on the structure than suggested by previous XRD studies. As stated previously,[11-13] the large variations of the H atomic coordinates are attributable to the large uncertainty in the location of H atoms by the XRD technique due to its non-spherical nature of the electron density and the small diffraction coefficient,[9,37,38] and/or H disorder (i.e., dynamic behavior or static disorder) in the crystal structures. This problem is reflected by the fact that the O-H bond length of 0.754 Å for the O10-H3 in probertite (Table S2) determined by XRD is significantly shorter than typical O-H bond lengths obtained from neutron diffraction studies of inorganic borates.[3,38]

4.2.^{11}B NMR shielding contributions

4.2.1. NMR shielding calculations. NMR experiments usually measure the chemical shifts relative to a specific reference, whereas theoretical calculations give the absolute shielding with respect to a bare nucleus. It is interesting to note that the calculated isotropic shielding (σ_{iso} or σ_{TOT}) between the periodic GIPAW and LAPW+LO methods are broadly similar, whereas those from the cluster hybrid-DFT technique are notably different (Table 2). Nevertheless, all theoretical calculations, including those from the cluster hybrid-DFT approach for ulexite, appear to well reproduce the shielding differences between $^{[3]}$B and $^{[4]}$B sites in both ulexite and probertite (Table 2). Moreover, the subtle differences of ~1 ppm between the two different $^{[3]}$B sites obtained from the ultra-high-field NMR experiments[11,12] are reproduced by all periodic calculations, but not by the cluster hybrid-DFT approach (Table 2). Closer examination shows that the differences in the calculated absolute shieldings at the $^{[3]}$B sites between ulexite and probertite from LAPW+LO for the optimized structures are small, consistent with those obtained from NMR experiments. The calculated absolute shieldings at the $^{[3]}$B sites from GIPAW for optimized structures, on the other hand, differ by as much as 4 ppm between ulexite and probertite, not observed in NMR experiments. Similarly, the differences of ~3 ppm in calculated absolute shieldings between ulexite and probertite from LAPW+LO for the original X-ray structures are too large in comparison with NMR experimental data. Therefore, the LAPW+LO method using optimized structures is obviously the best among those evaluated in this study.

The NMR tensor components corresponding to both $^{[3]}$B and $^{[4]}$B in the pentaborate minerals calculated by LAPW+LO (Table 3) also show little variations among the different $^{[3]}$B/$^{[4]}$B sites. The principal components of the ^{11}B paramagnetic shielding tensors in borates can be associated with the B-O bond directions as well as the mixing of the excited state with the ground state: σ^p_{XX} (perpendicular to B-O bonds) with σ to π^* excitations, σ^p_{YY} (parallel to B-O bonds) with n to π^*, and σ^p_{ZZ} with σ to σ^*.The directions of the unique σ^p_{ZZ} are approximately parallel to those of the principal nuclear quadrupolar component V_{ZZ} for $^{[3]}$B, but such a relationship is not evident for $^{[4]}$B.

Ideally, theoretical chemical shifts should be obtained by calculations of the absolute shielding of a reference compound. Unfortunately, the reference compound $BF_3.Et_2O$ used in ^{11}B NMR experiments[11-13] is liquid, which is not amendable to periodic DFT calculations of the types used in this study. Lakowski and Blaha obtained theoretical chemical shifts from the calculated absolute shieldings by using a reference taken from an unconstrained (slope different from -1) linear fit of the calculated absolute shieldings

versus experimental shifts.[16] This approach has been adopted herein to obtain theoretical chemical shifts from calculated absolute shielding in this study (Table 2). Specifically, the absolute shieldings from the periodic calculations of ulexite and probertite have been taken for unconstrained linear fits with the experimental chemical shifts. Data from each structure type were fitted separately to give an unbiased view, in the absence of calculations for a reference compound. As discussed above, the best agreements between the calculated chemical shifts and NMR experimental data for both ulexite and probertite are obtained from the LAPW+LO method for the optimized structures (Table 2).

Our LAPW+LO calculations for the optimized structures suggest that the chemical shifts among the three $^{[4]}$B sites in ulexite differ by as much as 1.6 ppm. The fact that these differences are not resolved in the NMR experiments - even at high fields - may simply be due to intrinsic peak broadening factors such as homo-nuclear dipolar coupling or structural disorder from imperfect crystallinity. On the other hand, fully resolved $^{[4]}$B peaks have been observed for minerals such as howlite[11] as well as partially resolved $^{[4]}$B signals in amorphous borates,[39-41] borosilicates,[42-44] and borophosphates.[45-47] Without an independent measure of the intrinsic line width it is difficult to discern whether this lack of resolution in NMR experiments is due to disorder or inaccurate calculations.

4.2.2. DOS calculations. The calculated electronic structures of ulexite[13] and probertite are characterized by the band gaps of 0.37 and 0.42 Ry (i.e. 5.0 and 5.7 eV), respectively (Fig. 2). Results of DOS calculations also show that O/2*s* does not interact significantly with Na/2*s*, Na/2*p* or Ca/4*s*. The topmost valence band (i.e., below the Fermi energy, E_F) is dominated by B/2*p* and O/2*p*, and the hybridization between the B/*p* and O/*p* states is evident in the corresponding partial DOS as well (Fig. 3).

4.2.3. Origins for magnetic shielding contributions. Results of DOS calculations and the electronic structures have been used to further examine the insensitivity of the NMR shielding at the B sites as well as the factors controlling the σ_{iso} differences between $^{[3]}$B and $^{[4]}$B in ulexite and probertite. Similar to ulexite,[13] DOS calculations decompose the energy windows for the two pentaborates, which may contribute to σ_{iso}, to the following: -∞ to -3.6 (core), -3.6 to -3.5 (Na/2*s*), -2.8 to -2.6 (Ca/3*s*), -1.5 to -1.45 (Na/2*p*), -1.45 to -1.1 (Ca/3*p* and O/2*s*), -0.7 to -0.45 (approximately B/2*s*), -0.45 to E_F (B/2*p*, interacting with Na/3*s*, Ca/4*s*, O/2*p* and H/1*s*) (Fig. 3). The calculated total and partial σ_{iso} contributions from the different energy windows for the various B sites in ulexite and probertite are summarized in Tables 4 and 5.

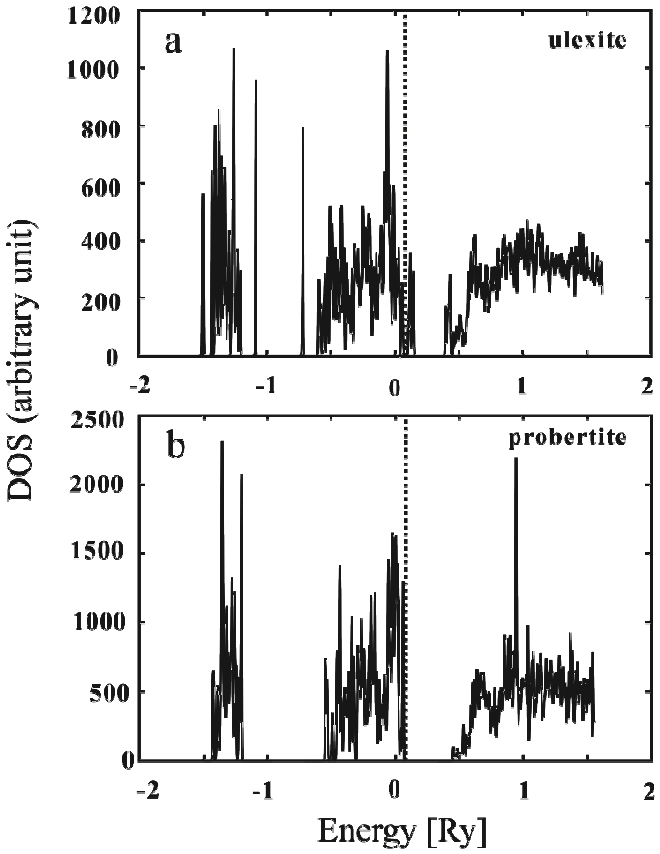

Fig. 2 Density of states (DOS) maps of (a) ulexite and (b) probertite. Dotted lines mark the Fermi level (E_F).

Table 2 Comparison of calculated ^{11}B magnetic shielding and experimental NMR chemical shifts in ulexite and probertite

Site	Exp.	Theoretical Calculations										
	δ_{iso}[§]	GIPAW^{O}		LAPW+LO^{O}		LAPW+LO^{X}		LAPW+LO^{K}		LAPW+LO^{D}		H-DFT[†]
	(ppm)	σ_{iso}	δ_{iso}	σ_{iso}	δ_{iso}	σ_{iso}	δ_{iso}	σ_{iso}	δ_{iso}	σ_{iso}	δ_{iso}	σ_{iso}
						Ulexite						
$^{[3]}$B2	18.8	76.6	20.0	74.9	18.8	78.7	19.9	74.5	19.6	74.1	19.7	83.4
$^{[3]}$B5	17.9	77.2	19.4	75.7	18.0	79.5	19.1	75.1	19.0	75.4	18.3	83.6
$^{[4]}$B1		94.4	2.4	93.1	0.6	96.5	2.1	92.0	1.6	92.2	0.9	101.3
$^{[4]}$B3	1.2	94.4	2.4	92.0	1.8	96.5	2.1	90.8	2.8	91.0	2.1	100.8
$^{[4]}$B4		94.0	2.8	91.5	2.2	95.9	2.8	90.6	3.0	90.7	2.5	100.9
χ	17.2	17.4	17.4	16.9	16.9	17.2	17.2	16.3	16.3	16.2	16.2	17.1
						Probertite						
$^{[3]}$B3	18.3	80.0	16.6	76.3	17.5	81.5	17.1	76.9	17.1	75.9	17.8	
$^{[3]}$B5	17.7	81.3	15.4	77.3	16.5	82.9	15.7	77.9	16.1	77.2	16.5	
$^{[4]}$B1		96.7	0.2	93.1	0.6	97.9	0.7	93.0	0.6	92.1	1.0	na
$^{[4]}$B2	1.3	96.5	0,4	92.8	1.0	98.3	0.3	93.4	0.1	92.5	0.6	
$^{[4]}$B4		96.4	0.5	92.8	1.0	98.0	0.6	93.3	0.3	92.3	0.8	
χ	16.7	15.9	15.9	16.1	16.1	15.9	15.9	15.8	15.8	15.7	15.7	

χ: average chemical shift or magnetic shielding differences between $^{[3]}$B and $^{[4]}$B; §: experimental data; [13]
O: calculated from the optimized structures; X: original XRD structures; K: optimized structures with K substituting for Na;
D: optimized structures with dehydration (i.e. all H_2O molecules removed); †: the cluster hybrid-DFT method; na, not available.

Journal Name RSCPublishing

ARTICLE

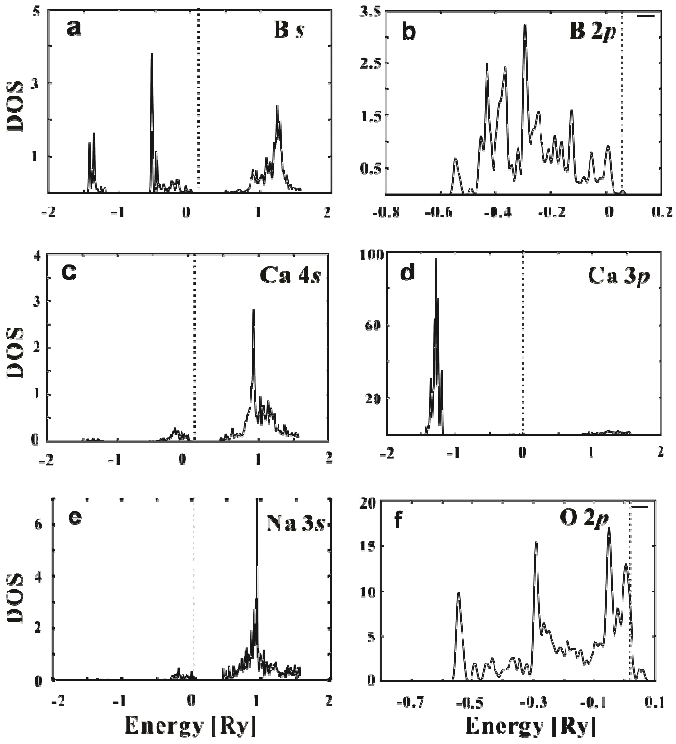

Fig. 3 Partial density of sates (DOS) maps for probertite: (a) B1/*s*; (b) B1/2*p*; (c) Ca/4*s*; (d) Ca/3*p*; (e) Na/3*s*; and (f) O3/2*p*. Dotted line marks the Fermi level (E_F).

The magnetic shielding arises mainly from the ground state currents and the currents excited from the ground states to their 1st-order perturbed states. The 1st-order perturbed states, which are caused by the external magnetic field, are the linear summation from the corresponding individual empty ground states (Eq. 3). As expected, the diamagnetic shielding at each B site results almost exclusively from the core states, i.e., the *s*-state orbitals, and the core contribution to σ_{iso} at all B sites is large at an approximately constant value of 165 ppm for both pentaborates investigated in this study (Tables 4 and 5). As Mason[48] pointed out, variations in the local diamagnetic term are usually negligible. Therefore, the contributions from the energy window below -3.6 Ry (i.e., the core states), which do not affect the magnetic shielding variations, can be safely ignored. Thus, interactions involved with the 1st-order perturbation of the ground states largely determine the variation of the magnetic shielding at a specific nucleus.[16-19]

In borates, the empty ground states of B and O are mainly the *p* orbitals, and interactions from *s* to *p* and *p* to *p* are the main causes for the shielding variations at each B site. Tables 4 and 5 clearly show that the interesting region starts only at -1.45 Ry (i.e., Ca/3*p* and O/2*s*), and the most important energy window contributing to σ_{iso} at the B sites ranges from -0.7 Ry to 0.033 Ry (E_F), which is a strongly broadened band containing all valence electrons such as B/2*s*, B/2*p*, Na/3*s*, Ca/3*p*, Ca/4*s*, O/2*p* and H/1*s* (Fig. 3, Tables 4 and 5). Among these valence states, the main contributions are from the upper B/2*s*, B/2*p* and O/2*p* bands, especially the latter two (i.e., the energy window between -0.45 and E_F) with the paramagnetic term

Table 3 Calculated[11]B magnetic shielding tensors in ulexite and probertite using the LAPW+LO method

Site	B1	B2	B3	B4	B5
Ulexite: XRD structure					
σ_{YY}	98.36	80.52	98.40	96.50	82.90
σ_{XX}	98.38	80.68	98.53	96.52	82.91
σ_{ZZ}	92.84	74.85	92.58	94.55	72.54
Ulexite: optimized structure					
σ_{YY}	94.78	77.66	93.67	93.41	78.85
σ_{XX}	94.79	77.86	93.80	93.47	78.87
σ_{ZZ}	89.78	69.24	88.47	87.68	69.47
Probertite: optimized structure					
σ_{YY}	94.75	79.90	94.05	89.85	79.62
σ_{XX}	94.75	81.33	95.23	89.18	81.19
σ_{ZZ}	88.88	70.58	90.08	99.21	68.0

Table 4 Calculated magnetic shielding contributions to the five B sites in ulexite using the LAPW+LO method

Site	[4]B1	[3]B2	[4]B3	[4]B4	[3]B5
Optimized ulexite without dehydration					
Core	165.2	165.1	165.2	165.2	165.1
Total	93.1	74.9	92.0	91.5	75.7
Sphere	85.5	75.2	80.4	84.7	58.1
σ_{TOT}-σ_{SPH}	7.60	-0.29	11.56	6.78	17.62
INST σ_{iso}	9.26	9.92	9.19	9.05	9.94
B/2*p*, O/2*p*	-59.3	-78.9	-68.8	-63.9	-87.1
B/2*s*	20.7	26.5	26.6	21.59	34.97
O/2*s*,Ca/3*p*	-14.1	-16.8	-13.4	-13.6	-16.9
∑	-53.4	-69.2	-55.5	-55.8	-69.0
Na/2*p*	0.01	0.04	0.01	0.02	0.00
Ca/3*s*	-0.09	-0.09	-0.09	-0.09	-0.09
Na/2*s*	-0.06	-0.07	-0.07	-0.07	-0.07
Optimized ulexite with complete dehydration					
Core	165.3	165.2	165.3	165.3	165.2
Total	92.2	74.1	91.0	90.7	75.4
Sphere	85.4	72.5	79.4	82.4	56.3
σ_{TOT}-σ_{SPH}	6.78	1.62	11.67	8.33	23.15
B/2*p*, O/2*p*	-58.0	-56.9	-72.1	-62.2	-67.1
B/2*s*	6.29	-9.61	18.7	8.71	1.79
O/2*s*,Ca/3*p*	-11.2	-6.49	-13.2	-12.6	-14.0
∑	-62.8	-72.5	-66.7	-66.1	-79.2
Na/2*p*	0.09	-6.1	3.81	1.82	0.99
Ca/3*s*	0.00	0.00	0.00	0.00	0.00
Na/2*s*	0.00	0.00	0.00	0.00	0.00

INST: interstitial contribution calculated from the current density integration outside the atomic sphere to the interstitial region; ∑ = B/2*p*+B/2*s*+O/2*p*+O/2*s*+Ca/3*p*

contributions ranging from -50 to -78 ppm. The contributions from the upper B/2*s* band are relatively small and are mostly of the diamagnetic type. Lower B/2*s* and semi-core metal-*s* bands lie at very low energies and thus hardly show any interaction with other orbitals (Fig. 3; Tables 4 and 5).

Therefore, contributions from the valence states dominate the variations of the magnetic shielding at the B sites, and the ^{11}B NMR shielding variations are almost completely determined by the B/2*p* and O/2*p* bands (Tables 4 and 5).

Almost all σ^p arises from the mixing of certain empty excited states with the occupied ground electronic states in the presence of an external magnetic field. Such dominance of the magnetic shielding variations by σ^p and so the importance of σ^p contributions were previous suggested by Mason,[48] because the calculated B/2*p* density matrix elements exhibit the best both $^{[3]}$B and $^{[4]}$B. The only excited states that can contribute to the paramagnetic term are those connected to the ground state by the correlations with the experimentally determined shielding for magnetic-dipole-allowed transitions. These transitions correspond to electron excitations between the orbital energy levels, which have nonzero matrix elements of the *x*, *y* and *z* components of the orbital angular momentum (such as rotation from p_x to p_y) and so involve a circulation of charge (charge rotation). These allowed transitions usually correspond to the lowest energy gap ΔE used in the approximation theory (Eq. 5), which is in terms of one-electron excitations such as *n* to σ^*, *n* to π^*, σ to π^*, or average over a few of them, and the most important orbitals are centered on the nucleus of interest.[48]

Table 5 Calculated magnetic shielding contributions to the five B sites in probertite using the LAPW+LO method

Site	$^{[4]}$B1	$^{[3]}$B2	$^{[4]}$B3	$^{[4]}$B4	$^{[3]}$B5
Core	165.3	165.3	165.2	165.3	165.2
Total	97.5	98.0	83.0	97.7	81.9
Sphere	80.9	83.4	67.8	80.4	60.1
σ_{TOT}-σ_{SPH}	16.7	14.6	15.2	17.3	20.8
INST σ_{iso}	15.5	15.4	16.9	15.2	16.8
B/2*p*, O/2*p*	-51.2	-50.0	-63.7	-51.0	-78.6
B/2*s*	8.39	7.74	9.85	9.00	23.1
O/2*s*,Ca/3*p*	-13.1	-13.5	-16.7	-13.1	-16.2
∑	-55.9	-55.7	-70.6	-55.1	-71.7
Na/2*p*	-0.27	-0.27	-0.27	-0.27	-0.27
Ca/3*s*	-0.17	-0.17	-0.17	-0.17	-0.17
Na/2*s*	0.00	0.00	0.00	0.00	0.00

INST: interstitial contribution calculated from the current density integration outside the atomic sphere to the interstitial region; ∑ = B/2*p*+B/2*s*+O/2*p*+O/2*s*+Ca/3*p*

Tables 4 and 5 also compare the magnetic shielding contributions only from inside the Muffin-Tin spheres (σ_{SPH}) with those calculated over all space (σ_{TOT}). This comparison shows that there are notable differences between σ_{TOT} and σ_{SPH} at each B site, ranging from 1.6 to 23.2 ppm (mostly >6.8 ppm) for ulexite, and from 14.6 to 20.8 ppm (mostly at ~15 ppm) for probertite. Obviously, the majority of σ_{iso} comes from the current inside the B atomic spheres (RMT^B = 1.29 a.u.), while the rest of the unit cell volume contributes to the remaining part. Therefore, such differences may be caused by the 'lattice' contribution (i.e., from the outside of the Muffin-Tin spheres), suggesting possible importance of contributions from interstitial spaces in crystals. This is not surprising that the 'lattice' contribution to σ_{iso} is important for B, because the lighter the element, the more covalent bonding is expected and the larger the lattice σ_{iso} contribution will become.[19] Therefore, in comparison with heavier nuclei and ionic compounds, the light nucleus B and the strongly covalent bonds in borates lead to large interstitial contributions. Consequently, the current density integration that goes beyond the atomic sphere to the interstitial region is necessary (Tables 4 and 5). Similarly, the lattice contributions to the EFG at the light element B sites are also significant in borates for the same reasons.[13] Of course, the main contribution to the absolute shielding comes from the relatively small volume around B (Tables 4 and 5).

Compared with the differences of σ_{TOT}-σ_{SPH}, the calculated interstitial shielding contributions (INST σ_{iso}) at each B site in the borates show minimal variations (Tables 4 and 5).Therefore, it is hard to interpret the large fluctuations in the differences of σ_{TOT}-σ_{SPH} by the interstitial contributions alone (Tables 4 and 5), especially for ulexite. One possible explanation is that there may exist a compensation mechanism between the local and distant interstitial shielding at the B sites. In such a compensation mechanism, the interstitial shielding from the local environment is compensated by that from more distant neighbors, which is responsible for the large σ_{TOT}-σ_{SPH}, and vice versa, as a result, the total interstitial contributions vary little. If assuming the interstitial contribution is ubiquitous and almost constant at all atoms in a given borate, the almost same shielding difference between $^{[3]}$B and $^{[4]}$B sites indicates that FBB alone (even without the next-nearest-neighbor H_2O included) already determines the B magnetic shielding that can be resolved by NMR experiments. As a matter of fact, Table 2 shows that the cluster with 25 atoms already reasonably produces the shielding differences between $^{[3]}$B and $^{[4]}$B sites in ulexite. This further manifests the localized character of the ^{11}B magnetic shielding parameter; as such, the cluster hybrid-DFT approach including only the atomic orbitals of the small 25-atom cluster can describe the shielding mechanism adequately. As a result, calculations using different methods such as GIPAW, LAPW+LO and cluster hybrid-DFT give almost the same σ_{iso} differences between $^{[3]}$B and $^{[4]}$B (Table 2).

In addition, the calculated ^{11}B NMR shieldings in both ulexite and probertite (Table 2) with K^+ substituting for Na^+ are similar to those of their normal Na counterparts, further confirming that the next-nearest-neighbor cations exert minimal influence. Our calculations do show, however, that these cations can *indirectly* affect the magnetic shielding at the B sites through the interstitial contributions (Tables 4 and 5).

Table 2 also gives the calculated ^{11}B NMR shielding results at the B sites in "dehydrated" ulexite and probertite. In comparison with the original structures, the calculated σ_{iso} values at the B sites change little after the removal of the water molecules (Table 2). Table 4 shows that the core, sphere, σ_{TOT}-σ_{SPH} at the B sites in the dehydrated ulexite are all closely comparable to those without dehydration, although the B/2*p*, O/2*p* (>-0.45), B/2*s* (-0.7, -0.45), O/2*s,* Ca/3*p* (-1.45, -1.1) energy windows between the two structures differ significantly. These differences are apparently compensated by the respective interstitial contributions to the magnetic shielding. These results demonstrate that the H_2O molecules and hydrogen bonds in ulexite do not exert any significant influence on the magnetic shielding at the B sites. This is further proof that ^{11}B NMR magnetic shielding in borates is a localized parameter, not sensitive to the structural variations beyond the first coordination sphere.

4.2.4. Origin for the isotropic shielding differences between $^{[3]}$B and $^{[4]}$B sites. Tables 4 and 5 also show that the magnitudes of the

magnetic shielding contributions from the different energy windows to σ_{iso} are different between the $^{[3]}$B and $^{[4]}$B sites. Although individual contributions from some states may have opposite signs for $^{[3]}$B and $^{[4]}$B, the summations of contributions from the two main energy windows of B/2*s*, B/2*p* and O/2*p* are almost constant at approximately -55 and -69 ppm for $^{[3]}$B and $^{[4]}$B in ulexite, and -55 and -70 ppm for $^{[3]}$B and $^{[4]}$B in probertite. Therefore, the shielding contributions from the B/2*s*, B/2*p* and O/2*p* almost determine the total σ_{iso} difference between $^{[3]}$B and $^{[4]}$B sites, which explains the experimental σ_{iso} differences of ~17 ppm between $^{[4]}$B and $^{[3]}$B sites in both pentaborates.

The σ_{iso} difference between $^{[3]}$B and $^{[4]}$B in borates may be rationalized by a simplistic *p*-orbital occupancy and electronic imbalance approach and how this affects the "excited state" paramagnetic contribution to the σ^p expressions by Eq. 5: [48]

$$\sigma^p = (-\mu_0/4\pi)(4\mu_B^2/\Delta E)[\langle r^{-3}\rangle_{np} P_i + \langle r^{-3}\rangle_{nd} D_i] \quad (5)$$

Where $\langle r^{-3}\rangle_{np}$ and $\langle r^{-3}\rangle_{nd}$ are the average distances from *p* and *d* orbitals to the central B atom, respectively. P_i and D_i represent the degrees of imbalance of the valence electrons in the *p* and *d* orbitals on the corresponding atom, respectively; σ^p is inversely or negatively proportional to P_i since D_i can be ignored for B sites in borates.[48]

In comparison with $^{[4]}$B, the *p*-type orbital at $^{[3]}$B is more vacant and its B p_z orbital is not full either. There is also a larger deficiency in the negative charge in p_z and a weaker π bonding relative to the σ-bonding p_x and p_y orbitals at the $^{[3]}$B sites.[13] Consequently, $^{[3]}$B sp^2 hybridization is less balanced (relative to the $^{[4]}$B sp^3 hybridization). As a result, it gives rise to more imbalances of the valence electrons around the central $^{[3]}$B and P_i will be at the maximum for the sp^2 occupancy, in contrast to a minimum for the sp^3 occupancy. As such, $^{[3]}$B sites show more deshielding (i.e., larger paramagnetic contributions to σ^p) than$^{[4]}$B. Therefore, the nuclear shielding at the $^{[3]}$B sites will be the lower in comparison with the higher shielding at $^{[4]}$B caused by the smaller σ^p in the latter. Intuitively, additional *p*-orbital occupancy would not only increase the electron density on the B atoms but also reduce the *p*-orbital imbalance, thus, both of which will increase the nuclear shielding. On the other hand, as π interactions with the otherwise vacant *p*-type orbitals of $^{[3]}$B is more prone than $^{[4]}$B, and since the shielding effects derive at least partly from the ground-state $p\pi$ donation and from the lone pair of the πelectrons of the neighboring O atoms, the σ^p contributions from the nearest-neighbor O atoms are more pronounced for $^{[3]}$B than that for $^{[4]}$B due to the readiness to form the $p\pi$ state.[48]

Another important reason for the isotropic shielding differences between $^{[3]}$B and $^{[4]}$B comes from the orbital distances to the central B atoms. The approximate Equation (5) for calculating the paramagnetic shielding also contains the proportional factor of $\langle r^{-3}\rangle$. Therefore, the closer the *p* electrons to the nucleus, the greater the paramagnetic terms are. As a result, the different contribution from the same energy windows to the $^{[3]}$B and $^{[4]}$B sites is at least partially caused by the different distances from the *sp* valence orbitals to the central B atoms, because the average B-O bond distances for $^{[3]}$B and $^{[4]}$B are 1.38 and 1.48 Å, respectively. The shorter B-O bond distances for $^{[3]}$B also lead to stronger antibonding [48] and thus more unoccupied orbitals (i.e., larger absolute P_i values for the $^{[3]}$B sites) and larger σ^p, less interstitial charge and lower valence density around the $^{[3]}$B atom sphere. Therefore, antibonding coupling contributes more negative paramagnetic shielding at the $^{[3]}$B sites.[19] Thus, orbital distances also affect the shielding contributions to σ_{iso} at the B sites and contribute to the total isotropic shielding difference between $^{[3]}$B and $^{[4]}$B as well.

The shielding difference range for B in borates may be stretched by the presence of low-lying excited states, since the approximate Equation (5) for paramagnetic shielding also contain the proportional factor of the excitation energy $(\Delta E)^{-1}$.The smaller $(\Delta E)^{-1}$, the greater the paramagnetic terms will be (Eq. 5). Increased shielding at the B sites may also be associated with the stabilization of the *n* orbital, when the low-lying excited states do not compensate. On the other hand, deshielding at the B sites may occur when coordination involves (π) back-bonding.[48] Therefore, there are multiple factors contributing to the σ_{iso} difference between $^{[3]}$B and $^{[4]}$B in borates, among which the P_i value associated with different types of B-O *sp* hybridization as well as the different distances from the *sp* valence orbitals to the central B atoms are shown to be the main factors.

Conclusions

The optimized structures of ulexite and probertite, in comparison with their counterparts from previous X-ray diffraction studies, have been shown to produce more accurate predictions for not only ^{11}B nuclear quadrupolar parameters (C_Q and η) but also the magnetic shieldings at the five distinct B sites each. In particular, periodic LAPW+LO calculations from the optimized structures have been shown to best reproduce the differences in ^{11}B chemical shifts between $^{[3]}$B and $^{[4]}$B in both pentaborates and confirm the subtle variations between the two distinct $^{[3]}$B sites in each mineral resolved in the ultra-high-field NMR spectra. Density of state (DOS) calculations also show that the magnetic shielding variations among the different B sites in ulexite and probertite are determined mainly by the interactions with the nearest-neighbor O atoms involving B/2*s*, B/2*p* and O/2*p*, whereas next-nearest-neighbor cations and H_2O molecules exert little effects. The total σ_{iso} differences between $^{[3]}$B and $^{[4]}$B in ulexite and probertite are caused by multiple factors, especially the *sp* hybridization properties.

Acknowledgements

The authors are very grateful to Prof. Christer Aakeroy and three reviewers for incisive criticisms and helpful suggestions. We also thank Drs. Robert Laskowski and Peter Blaha for insightful discussions and helpful instructions for magnetic shielding calculations using WIEN2k. BZ received a research grant of the "One Hundred People Plan" provided by Chinese Academy of Sciences for this study. This research has been enabled by the use of computing resources provided by WestGrid and Compute Canada. SK thanks the Canada Foundation for Innovation (CFI) and the Manitoba Research Innovation Fund for infrastructure support. SK and VKM are grateful to the Natural Sciences and Engineering Research Council (NSERC) of Canada for operating funds and a postgraduate scholarship, respectively.

Notes and references

[a]College of Materials Science and Engineering, Tongji University, China, 21000.

[b]Qinghai Institute of Salt Lakes, Chinese Academy of Sciences, China, 810008.

[c]Department of Chemistry, University of Manitoba, Winnipeg, Manitoba, Canada R3T 2N2.

[d]Physics Department and Shanghai Key Laboratory of Magnetic Resonance, East China Normal University, Shanghai 200062, China.

Journal Name

RSCPublishing

ARTICLE

[e]Department of Geological Sciences, University of Manitoba, Winnipeg, Manitoba, Canada R3T 2N2.
[f]Department of Geological Sciences, University of Saskatchewan, Saskatoon, Saskatchewan, Canada S7N 5E2.

† Current address: Francis Bitter Magnet Laboratory, Department of Chemistry, Massachusetts Institute of Technology, Cambridge, MA 02139 USA

* Corresponding author: Email: yuanming.pan@usask.ca; Tel: (306) 966-5699; Fax: (306) 966-8593

1 A. Lussier, P. M. Aguiar, V. K. Michaelis, S. Kroeker and F. C. Hawthorne, Am. Mineral., 2009, 94, 785-792.
2 B. J. Greer and S. Kroeker, Phys. Chem. Chem. Phys., 2012, 14 , 7375-7383.
3 C. Bonhomme, C. Gervais, F. Babonneau, C. Coelho, F. Pourpoint, T. Azaïs, S. E. Ashbrook, J. M. Griffin,J. R. Yates, F. Mauri and C. J. Pickard, 2012, Chem. Rev., 112, 5733-5779.
4 T. Charpentier, Solid State Nucl. Magn.Reson., 2011, 40, 1-20.
5 A. Sadoc, M. Body, C. Legein, M. Biswal, F. Fayon, X. Rocquefelte and F. Boucher, Phys. Chem. Chem. Phys., 2011, 13, 18539-18550.
6 R. K. Harris, S. Cadars, L. Emsley, J. R. Yates, C. J. Pickard, R. K. R. Jetti and U. J. Griesser, Phys. Chem. Chem. Phys., 2007, 9, 360-368.
7 P. Bray, J. Edwards, J. O'Keefe, V. Ross and I. Tatsuzaki, J. Phys. Chem., 1961, 35, 435-442.
8 G. L. Turner, K. A. Smith, R. J. Kirkpatrick and E. Oldfield, J. Magn. Reson., 1986, 67, 544-550.
9 M. R. Hansen, G. K. Madsen, H. J. Jakobsen and J. Skibsted, J. Phys. Chem., 2005, A109, 1989-1997.
10 O. L. G. Alderman, D. Iuga, A. P. Howes, K. J. Pike, D. H. and R. Dupree, Phys. Chem. Chem. Phys., 2013, 15, 8208-8221.
11 B. Zhou, V. K. Michaelis, S. R. Giesbrecht, S. Kroeker, B .L. Sherriff, Z. Sun, Y. Yao and Y. Pan, Phys. Chem. Miner., 2012, 39, 373-383.
12 B. Zhou, V. K. Michaelis, Y. Pan, Y. Yao, K. T. Tait,B. C. Hyde, J. E. C. Wren, B. L. Sherriff and S. Kroeker, Am. Mineral., 2012, 97, 1858-1865.
13 B. Zhou, V. K. Michaelis, J. E. C. Wren, S. Kroeker, Y. Yao, B. L. Sherriff and Y. Pan, CrystEngComm., 2013, 98, 8739-8747.
14 S. Ghose, C. Wan and J. R. Clark, Am. Mineral., 1978, 63, 160-171.
15 S. Menchetti, C. Sabelli and R. Trosti-Ferroni, Acta Cryst., 1982, B38, 3072-3075.
16 R. Laskowski and P. Blaha, Phys. Rev., 2014, B89, 014402.
17 R. Laskowski and P. Blaha, Phys. Rev., 2013, B87, 195130.
18 R. Laskowski and P. Blaha, Phys. Rev., 2012, B85, 035132.
19 R. Laskowski and P. Blaha, Phys. Rev., 2012, B85, 245117.
20 A. Zheng, S.-B. Liu and F. Deng, J. Phys. Chem., 2009, C113, 15018-15023.
21 A. Zheng, B. Han, B. Li, S.-B. Liu and F. Deng, Chem. Comm., 2012, 48, 6936-6938.
22. P. He, J. Xu, V. V. Terskikh, A. Sutrisno, H.-Y. Nie and Y. Huang, J. Phys. Chem., 2013, C113, 16953-16960.
23 A. Sutrisno, L. Liu, J. Dong and Y. Huang, J. Phys. Chem., 2012, C116, 17070-17081.
24 P. Feibelman, B. Hammer, J. K. Nørskov, F. Wagner, M. Scheffler, R. Stumpf, R. Watwe and J. Dumesic, J. Phys. Chem., 2001, B105, 4018-4025.
25 P. Blaha, K. Schwarz and P. Sorantin, Comput. Phys. Commun., 1990, 59, 39-415.
26 P. Blaha, D.J. Singh, P. I. Sorantin and K. Schwarz, Phys. Rev., 1992, B46, 1321-1325.
27 P. Blaha, K. Schwarz, G. K. Madsen, D. Kvasnicka and J. Luitz, WIEN2k, ISBN 3-9501031-1-2, Technische Universität, Wien, 2001.
28 W. Kohn and L. J. Sham, Phys. Rev., 1965, 140(4A), 1133-1138.
29 J. B. Foresman and A. Frisch, Gaussian Inc., Exploring chemistry with electronic structure methods, 2th Edition, Pittsburgh, 1996.
30 W. G. Richards and J. A. Horsley, Oxford University Press, Ab initio molecular orbital calculations for chemists, London, 1970.
31 J. A. Tossell, J. Chem. Phys., 1986, 84, 369-374.
32 J. A. Tossell, Am. Mineral., 1993, 78, 16-22.
33 J. A. Tossell, Phys. Chem. Miner., 1999, 27, 70-80.
34 H. Koller, G. Engelhardt, A.P.M. Kentgens and J. Sauer, J. Phys. Chem., 1994, 98, 1544-1551.
35 S. Dong, R. Ida and G. Wu, J. Chem. Phys., 2000, 104A, 11194-11202.
36 K. Yamada, S. Dong and G. Wu, J. Am. Chem. Soc., 2000, 122, 11602-11609.
37 P. C. Burns and F. C. Hawthorne, Can. Mineral., 1993, 31, 297-304.
38 P. C. Burns and F. C. Hawthorne, Can. Mineral., 1994, 32, 885-894.
39 V. K. Michaelis, P. M. Aguiar and S. Kroeker, J. Non-Cryst. Solids, 2007, 353, 2582-2590.
40 V. K. Michaelis and S. Kroeker, Phys. Chem. Glasses: Eur. J. Glass Sci. Technol. B, 2009, 50 (4), 249-252.
41 S. Kroeker, P. M. Aguiar, A. Cerquiera, J. Okoro, W. Clarida, J. Doerr, M. Olesiuk, G. Ongie, M. Affatigato and S. A. Feller., Phys. Chem. Glasses: Eur. J. Glass Sci. Technol. B, 47 (4), 2006, 393-396.
42 L.-S. Du and J. F. Stebbins, J. Non-Cryst. Solids, 2003, 315, 239-255.
43 L.-S. Du and J. F. Stebbins, Chem. Mater., 2003, 15, 3913-3921.
44 L.-S. Du and J. F. Stebbins, J. Phys. Chem., 2003, B107, 10063-10076.
45 S. Elbers, W. Strojek, L. Koudelka and H. Eckert, Solid State Nucl. Magn.Reson., 2005, 27, 65-76.
46 M. T. Rinke and H. Eckert, Phys. Chem. Chem. Phys., 2011, 13, 6552-6565.

47 V. K. Michaelis, P. Kachhadia and S. Kroeker, Phys. Chem. Glasses: Eur. J. Glass Sci. Technol. B, 2013, 54 (1), 20-26.
48 J. Mason, Multinuclear NMR, Plenum Press, New York and London, 1987.